Fuel 237 (2019) 1244–1253

Contents lists available at ScienceDirect

Fuel

journal homepage: www.elsevier.com/locate/fuel

Full Length Article

Ni supported $Ce_{0.9}Sm_{0.1}O_{2-\delta}$ nanowires: An efficient catalyst for ethanol steam reforming for hydrogen production

Thenner S. Rodrigues[a], Arthur B.L. de Moura[a], Felipe A. e Silva[a], Eduardo G. Candido[a], Anderson G.M. da Silva[b], Daniela C. de Oliveira[c], Jhon Quiroz[b], Pedro H.C. Camargo[b], Vanderlei S. Bergamaschi[a], João C. Ferreira[a], Marcelo Linardi[a], Fabio C. Fonseca[a,*]

[a] Instituto de Pesquisas Energéticas e Nucleares, IPEN-CNEN, São Paulo, SP 05508-000, Brazil
[b] Departamento de Química Fundamental, Instituto de Química, Universidade de São Paulo, Av. Prof. Lineu Prestes, 748, 05508-000 São Paulo, SP, Brazil
[c] Centro Nacional de Pesquisa em Energia e Materiais, Laboratório Nacional de Luz Síncrotron, 13083-970 Campinas, SP, Brazil

GRAPHICAL ABSTRACT

ARTICLE INFO

Keywords:
$Ni/Ce_{0.9}Sm_{0.1}O_{2-\delta}$ nanowires
Ethanol steam reforming
Hydrogen production
Nanostructured catalyst
Controlled and superior properties

ABSTRACT

We reported herein the synthesis in high yields (> 97%) of $Ce_{0.9}Sm_{0.1}O_{2-\delta}$ nanowires displaying well-defined shape, size, and composition by a simple, fast, and low-cost two-step hydrothermal method. The $Ce_{0.9}Sm_{0.1}O_{2-\delta}$ nanowires synthesis was followed by the wet impregnation of Ni without the utilization of any stabilizing agent. The $Ni/Ce_{0.9}Sm_{0.1}O_{2-\delta}$ nanowires showed higher surface area, high concentration of oxygen vacancies at surface, and finely dispersed Ni particles with significantly higher metallic surface area as compared with catalysts prepared from commercial materials with similar compositions. Such unique and improved properties are reflected on the catalytic performance of the $Ni/Ce_{0.9}Sm_{0.1}O_{2-\delta}$ nanowires towards ethanol steam reforming. The nanowires exhibited high yields for hydrogen production (~60% of selectivity) and an exceptional stability with no loss of activity after 192 h of reaction at 550 °C. The reported results provide insights and can inspire high-yield production of nanostructured catalysts displaying controlled and superior properties that enable practical applications in heterogeneous catalysis.

1. Introduction

Biomass derived ethanol is an available and efficient fuel with a well-developed infrastructure for both production and distribution in countries such as USA and Brazil [1]. Ethanol is a well established biofuel for combustion engines and, more recently, increasing attention

* Corresponding author.
E-mail address: fabiocf@usp.br (F.C. Fonseca).

https://doi.org/10.1016/j.fuel.2018.10.053
Received 18 June 2018; Received in revised form 5 October 2018; Accepted 8 October 2018

has been given to the use of ethanol in fuel cells and as a renewable source for hydrogen production [2–4]. In order to supply the global demand for hydrogen (H_2), the steam reforming of hydrocarbons (such as methane) using mostly nickel-based catalysts has been widely employed [4–10]. However, the increased demand for more sustainable and greener methods has ramped up ethanol steam reforming because of the large availability, relatively low cost, and superior reactivity of ethanol as compared to methane [11–13].

Due to the reaction mechanism, noble metals such as Rh would be the best catalysts for ethanol steam reforming, but their high costs has shifted the attention to nickel and cobalt-based catalysts [14]. Such transition metals show high activities toward ethanol steam reforming, but suffer from strong deactivation because the extensive carbon deposition [15]. Thus, in order to overcome this limitation, many catalysts based on Ni and Co and metal oxides have been developed, which proved to be the most promising candidates in terms of activity and selectivity to H_2 [15–20].

Concerning the support, cerium oxide (CeO_2) has demonstrated to be the one of the best options for improving ethanol steam reforming. More specifically, CeO_2 presents an unique intrinsic oxygen storage capability and oxygen mobility at its surface due to the presence of Ce^{3+} and Ce^{4+} ions, which are essential to prevent deposition of carbon compounds that deactivate the employed catalysts. [21–24] Previous studies have demonstrated that these exceptional properties can be significantly enhanced by doping CeO_2 catalysts with rare-earth oxides (samarium, gadolinium, lanthanium, among others), leading to non-stoichiometric compounds displaying even higher oxygen storage capability and oxygen mobility at their surface [20,24–28]. The synthesis of CeO_2-based materials displaying controlled properties (size, shape, and composition) is considered as an excellent strategy for the enhancement of their catalytic performances. [29–32] In the past few years, great developments linking the nanostructure of CeO_2 supports with catalytic performance. In this context, one-dimensional CeO_2 nanostructured materials have received a tremendous amount of attention due to their unique properties derived from low dimensionality and high surface area [33].

In this present study, we demonstrated the high-yield synthesis of samarium-doped ceria nanowires as a novel catalyst support displaying outstanding performances towards ethanol steam reforming. Due to the high specific surface area, small thickness, and high concentration of oxygen vacancies of the Sm doped-ceria nanowires, $Ni/Ce_{0.9}Sm_{0.1}O_{2-\delta}$ catalysts displayed improved performance towards the ethanol steam reforming compared to their analogue catalysts prepared from commercial doped-ceria. Furthermore, this nanostructured catalyst displayed outstanding long-term stability under practical conditions of a typical steam reforming system.

2. Experimental

2.1. Materials and instrumentation

Analytical grade cerium (III) nitrate hexahydrate ($Ce(NO_3)_3{\cdot}6H_2O$, 99.5%, Sigma-Aldrich), samarium (III) nitrate hexahydrate ($Sm(NO_3)_3{\cdot}6H_2O$, 99.5%, Sigma-Aldrich), sodium hydroxide (NaOH, 99%, Sigma-Aldrich), nickel (II) nitrate hexahydrate ($Ni(NO_3)_2{\cdot}6H_2O$, 99.5%, Sigma-Aldrich), cerium (IV) oxide (CeO_2, 99.9%, Sigma-Aldrich), samarium (III) oxide (Sm_2O_3, 99.9%, Sigma-Aldrich), and ethanol (C_2H_6O, 99.5%, Sigma-Aldrich), were used as received.

Scanning electron microscopy (SEM) images were obtained using a JEOL field emission gun microscope JSM 6330F operated at 5 kV. Samples were prepared by drop-casting an aqueous suspension containing the nanostructures over a silicon wafer, followed by drying under ambient conditions. The high-resolution transmission electron microscopy (HRTEM) images were obtained with a Tecnai FEI G20 microscope operated at 200 kV. Samples for HRTEM, were prepared by drop-casting an aqueous suspension of the materials over a carbon-coated copper grid, followed by drying under ambient conditions. The Ni weight percentages were measured by inductively coupled plasma optical emission spectrometry (ICP-OES) using a Spectro Arcos equipment. Specific surface areas were determined by the Brunauer-Emmett-Teller equation (BET method) using a Quantachrome ChemBET-Pulsar instrument equipped with a thermal conductivity detector. Typically, 0.05 g of a catalyst was pretreated with He flow at 400 °C for 4 h and then cooled down to room temperature. Temperature-programmed reduction with hydrogen (H_2-TPR) and CO-chemisorption studies were carried out in the Quantachrome ChemBET-Pulsar instrument equipped with a thermal conductivity detector. Typically, 0.05 g of a catalyst was pretreated with He flow at 120 °C for 1 h and then cooled down to room temperature. The TPR profiles were obtained between 50 and 1100 °C in a flow of 10% H_2/N_2, the temperature increasing linearly at a rate of 10 °C min^{-1}. The CO chemisorption data and carbon monoxide temperature-programmed desorption profiles (CO-TPD) were carried out on both fresh and spent catalysts. The CeSm-based samples without addition of Ni were also analyzed for comparison to ensure that only Ni is able to adsorb CO under the conditions used. Thus, the experiments were performed by CO pulse chemisorption at 50 °C using pulses of 5% CO in He. Prior to the chemisorption, 0.05 g of the catalyst was pretreated at 450 °C under a 10% H_2/N_2 flow, the temperature increased linearly at a rate of 10 °C min^{-1} and kept at 450 °C for 1 h, and then cooled down to 50 °C. Sequentially, temperature programed desorption was performed by heating in a stream of He at 75 mL min^{-1} between 50 and 1100 °C with heating rate of 10 °C min^{-1}. The X-ray diffraction (XRD) data were obtained using a Rigaku-Miniflex II equipment and Cu K-alpha radiation. The diffraction patterns were measured in the range of 20 − 90° 2θ with a 1° min^{-1} angular speed scan. Thermogravimetric (TGA) measurements were carried out using a Setaram-LabSys equipment in the 25–1000 °C temperature range using a heating rate of 5 °C min^{-1} under nitrogen flow. Raman spectra were collected using a in a Renishaw InVia Reflex coupled to a Leica DM 2500 M microscope and a CCD detector. The laser excitations used were 632.8 nm (He/Ne source) and the objective was a 50 × objective (NA = 0.9). X-ray photoelectron spectroscopy (XPS) data of the samples was obtained with an SPECSLAB II (Phoibos-Hsa 3500 150, 9 channeltrons) SPECS spectrometer, with Al Kα source (E = 1486.6 eV) operating at 12 kV, pass energy (Epass) = 40 eV, 0.1 eV energy step and acquisition time of 1 s per point. The samples were placed on stainless steel sample-holders and were transferred under inert atmosphere to the XPS pre-chamber and held there for 2 h in a vacuum atmosphere. The residual pressure inside the analysis chamber was $\sim 1 \times 10^{-9}$ Torr. The binding energies (BE) of the Ce 3d and O 1s spectral peaks were referenced to the C 1s peak, at 284.5 eV, providing accuracy within ± 0.2 eV. The oxygen vacancies or surface oxygen were estimated by deconvolution of the O (1s) peak into three spectral contributions: the low binding energy peak (529.9–529.5 eV) ascribed to lattice oxygen O_L, the medium binding energy peak (532.0–531.4 eV) assigned to oxygen vacancies or surface oxygen ions O_S and the high binding energy peak at 533.9 ev associated with adsorbed molecular water O_W. The percentage in surface of the different oxygen species was obtained by the Gaussian peak fit procedure according to the software supplied by CasaXPS.

2.2. Synthesis of $Ni/Ce_{0.9}Sm_{0.1}O_{2-\delta}$ nanowires

The first step was the synthesis of the $Ce_{0.9}Sm_{0.1}O_{2-\delta}$ nanowires by a hydrothermal method [34]. Typically, 19.6 g of NaOH were dissolved in 35 mL of deionized water and then transferred to a 100 mL Teflon-lined stainless steel autoclave. Then, 6.25 g of $Ce(NO_3)_3{\cdot}6H_2O$ and 0.71 g of $Sm(NO_3)_3{\cdot}6H_2O$ dissolved in 5 mL of deionized water were gradualy added to the NaOH solution under vigorous magnetic stirring. The autoclave was heated at 110 °C for 24 h and then allowed to cool down to room temperature. Synthesis of pure CeO_2 and Sm_2O_3 nanowires for comparison was carried out following the same protocol. For such materials, 6.95 g of $Ce(NO_3)_3{\cdot}6H_2O$ and 7.11 g of $Sm(NO_3)_3{\cdot}6H_2O$

were employed, respectively. After their synthesis, the products were collected by centrifugation and washed five times with water (40 mL) and three times with ethanol (40 mL) by successive rounds of centrifugation and removal of the supernatant. The as prepared materials were then dried at 120 °C for 2 h in air. The incorporation of Ni (1 wt%) onto the obtained nanowires was performed using a wet impregnation approach [35]. Typically, 6.88 mL of a $Ni(NO_3)_2{\cdot}6H_2O$ aqueous solution (25 mM) was added to a beaker containing 1*g* of the respective nanowire and 30 mL of water. The resulting mixture was sonicated at room temperature for 30 min and then stirred at 70 °C until dryness under magnetic stirring. Finally, the resulting product was dried at 120 °C for 2 h under air and calcined at 450 °C for 2 h with heating rate of 10 °C min^{-1}. This temperarute was determined based on the TGA analysis (Fig. S1), in which no significant weight loss was observed with increasing temperature.

2.3. Catalytic experiments: Ethanol steam reforming

Catalytic experiments were carried out at atmospheric pressure in a fixed-bed quartz tubular reactor, 5 mm of inner diameter, packed with 100 mg of catalyst placed in a vertical oven equipped with a thermocouple for the control of temperature. Prior to reaction, the catalysts were heat-treated under hydrogen at 450 °C for 1 h with a flow rate of 30 mL min^{-1}. Water and ethanol were fed into the reactor using a system with two saturators to obtain a H_2O/CH_3CH_2OH molar ratio = 3. Nitrogen was used as carrier gas at a total flow rate of 20 mL min^{-1}. Herein, the residence time and gas hourly space velocity corresponded to 0.59 s and 6115 h^{-1}, respectively. The reactants and the reaction products were analyzed by gas chromatograph (Agilent 7890A), equipped with a thermal conductivity detector (TCD) and a flame ionization detector (FID) connected in series.

The catalytic performances were evaluated by the profiles of conversion of ethanol ($C_{CH3CH2OH}$) and selectivity for the obtained products as function of the reaction time: hydrogen (S_{H2}), carbon dioxide (S_{CO2}), carbon monoxide (S_{CO}), methane (S_{CH4}), acetone ($S_{CH3(CO)CH3}$), acetaldehyde (S_{CH3CHO}), and ethene (S_{C2H4}), which were calculated by the Eqs. (1)–(8) as follows [36]. In addition, Eq. (9) shows an unique general formula to determine the selectivity of C-products.

$$C_{CH_3CH_2OH}\,[\%] = \frac{(mol_{CH_3CH_2OH,in} - mol_{CH_3CH_2OH,out})}{mol_{CH_3CH_2OH,in}} \times 100 \quad (1)$$

$$S_{H_2}\,[\%] = \frac{(mol_{H_2}/6)}{(mol_{CH_3CH_2OH,in} - mol_{CH_3CH_2OH,out})} \times 100 \quad (2)$$

$$S_{CO_2}\,[\%] = \frac{(mol_{CO_2}/2)}{(mol_{CH_3CH_2OH,in} - mol_{CH_3CH_2OH,out})} \times 100 \quad (3)$$

$$S_{CO}\,[\%] = \frac{(mol_{CO}/2)}{(mol_{CH_3CH_2OH,in} - mol_{CH_3CH_2OH,out})} \times 100 \quad (4)$$

$$S_{CH_4}\,[\%] = \frac{(mol_{CO_4}/(2))}{(mol_{CH_3CH_2OH,in} - mol_{CH_3CH_2OH,out})} \times 100 \quad (5)$$

$$S_{CH_3(CO)CH_3}\,[\%] = \frac{\left(mol_{CO_3(CO)CH_3}/\left(\frac{2}{3}\right)\right)}{(mol_{CH_3CH_2OH,in} - mol_{CH_3CH_2OH,out})} \times 100 \quad (6)$$

$$S_{CH_3CHO}\,[\%] = \frac{(mol_{CH_3CHO})}{(mol_{CH_3CH_2OH,in} - mol_{CH_3CH_2OH,out})} \times 100 \quad (7)$$

$$S_{C_2H_4}\,[\%] = \frac{(mol_{C_2H_4})}{(mol_{CH_3CH_2OH,in} - mol_{CH_3CH_2OH,out})} \times 100 \quad (8)$$

$$S_X\,[\%] = \frac{\left(mol_X/\left(\frac{2}{C}\right)\right)}{(mol_{CH_3CH_2OH,in} - mol_{CH_3CH_2OH,out})} \times 100 \quad (9)$$

where X represents the formed carbon-based products (CO_2, CO, CH_4, C_2H_4, CH_3CHO, and CH_3COCH_3) and C is the number of carbon atoms in these respective species.

3. Results and discussion

The first step was the synthesis of the catalyst, which is based on Ni supported $Ce_{0.9}Sm_{0.1}O_{2-\delta}$ nanowires. The synthesis of the nickel-supported $Ce_{0.9}Sm_{0.1}O_{2-\delta}$ nanowires can be divided in a two-step approach, as depicted in the Fig. S2. In the first step, $Ce_{0.9}Sm_{0.1}O_{2-\delta}$ nanowires displaying well-defined sizes and shapes were obtained (SEM, HRTEM, and STEM-EDX images are shown in Fig. S3). Herein, we were inspired by a simple and robust hydrothermal method previously employed for the fabrication of CeO_2 nanowires [37]. In this case, we performed the doping of the CeO_2 matrix with a rare earth cation (Sm^{3+}) during the synthesis by simply mixing their respective precursor salts into a unique aqueous solution. The formation of a CeO_2 structure containing the Sm atoms homogeneously distributed was promoted upon contact with the alkaline solution under vigorous stirring. The doping of CeO_2 matrix was performed using the atomic proportion of 9:1 between Ce and Sm, respectively, and can described by following chemical Eqs. (10) and (11) [38]:

$$0.9Ce^{3+}_{(aq)} + 0.1Sm^{3+}_{(aq)} + 3.9OH^{-}_{(aq)} + xH_2O \rightarrow 0.9Ce(OH)_4.xH_2O_{(s)} + 0.1Sm(OH)_3.xH_2O_{(s)} \quad (10)$$

$$0.9Ce(OH)_4.xH_2O_{(s)} + 0.1Sm(OH)_3.xH_2O_{(s)} \rightarrow Ce_{0.9}Sm_{0.1}O_{2-\delta(s)} + xH_2O_{(g)} \quad (11)$$

The obtained $Ce_{0.9}Sm_{0.1}O_{2-\delta}$ nanowires were 12.6 ± 2.2 nm in width and could be synthesized in high yields (> 97%), which led to the formation of ~2.8 g of nanowires. Phase-contrasted HRTEM images indicated that the $Ce_{0.9}Sm_{0.1}O_{2-\delta}$ nanowires were single-crystalline with ~0.32 nm lattice spacings assigned to the growth direction along the [1 1 0] axis (Fig. S3C), in agreement with structure of the CeO_2 structure [37,39,40]. Moerover, energy dispersive X-ray spectroscopy (STEM-EDX) mapping (Fig. S3D–E) confirmed that both Ce and Sm are uniformly distributed over the entire extension of the nanowires, indicating that our first goal was successfully achieved. For comparison, we also prepared pure CeO_2 and Sm_2O_3 nanowires using the same hydrothermal method, and SEM, HRTEM, and STEM images are shown in Fig. S3A–D.

In the second step, the obtained $Ce_{0.9}Sm_{0.1}O_{2-\delta}$ nanowires were used as a high-surface area support for the incorporation of nickel aimed at ethanol steam reforming reaction [13]. Ni was added by a wet impregnation route, which is an effective procedure to high metallic dispersion if many steps of preparation are controlled. Such route was previously demonstrated as an effective procedure for the fabrication of supported catalysts displaying uniform dispersion of the metallic phase over the ceramic support surface [23,35,41,42]. By following this impregnation route, $Ni/Ce_{0.9}Sm_{0.1}O_{2-\delta}$ nanowire catalysts with Ni loading corresponding to 1 wt% (confirmed by the ICP-OES analysis) were prepared. As depicted in the Fig. 1A–C, no changes in the morphology or agglomeration of the $Ce_{0.9}Sm_{0.1}O_{2-\delta}$ nanowires were observed after Ni impregnation, indicating the robustness of this support. As revealed by SEM and HRTEM images, the formation of Ni NPs at the surface of the nanowires could not be detected. Interestingly, in STEM-EDX images (Fig. 1D–G), nickel apperared to be uniformly distributed over the entire structure. This feature can be associated with the high surface area of the $Ce_{0.9}Sm_{0.1}O_{2-\delta}$ nanowires support, which provide a large number of nucleation sites for the metallic nanoparticles, and a careful experimental control during impregnation. The efficient sonication step and the slow solvent evaporation at low temperatures (usually < 80 °C) are important for an efficient impregnation of Ni over the nanowires [43]. Thus, finely dispersed nanoparticles were anchored to the surface of nanowires and, consequently, a uniform coating of the support was promoted. Such properties maximize the available metallic surface area

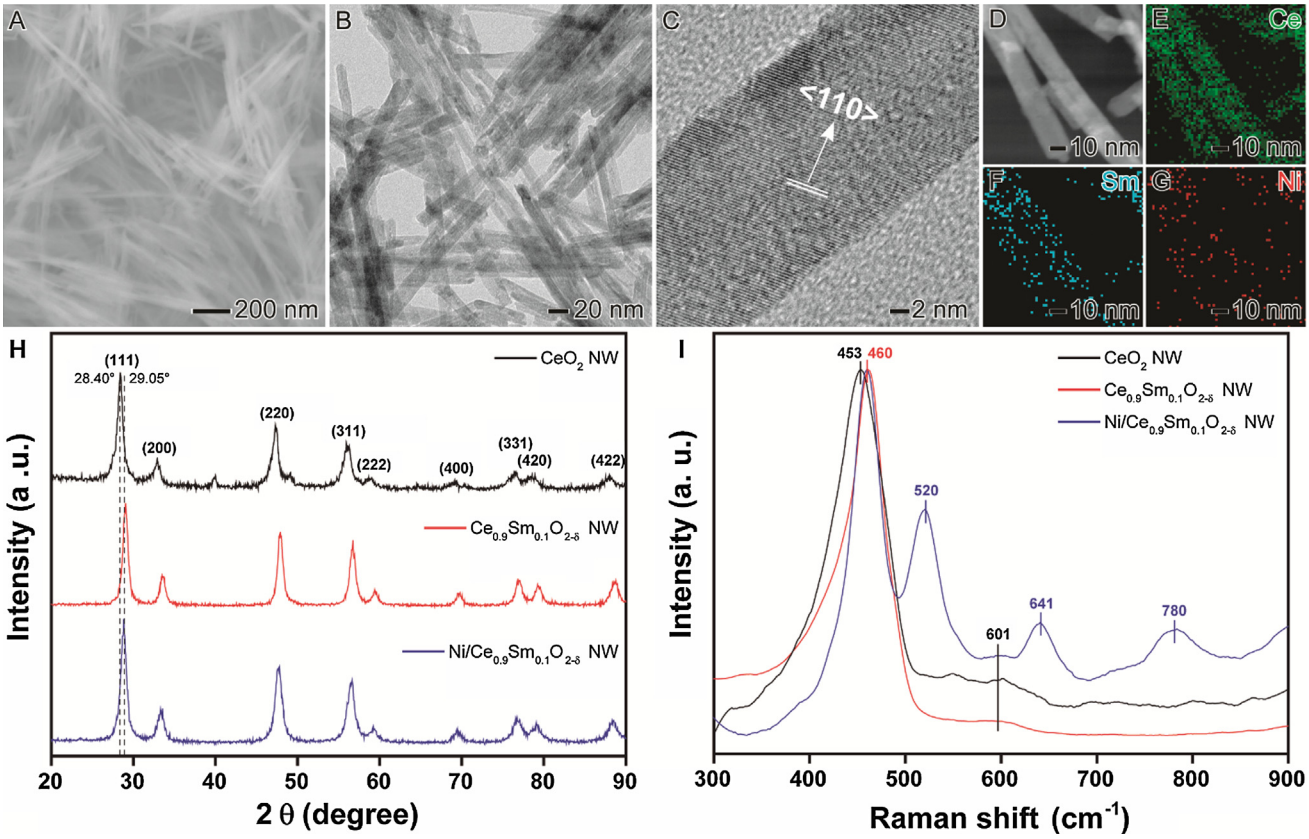

Fig. 1. (A) SEM, (B-C) HRTEM, and (D-G) STEM-EDX images of $Ni/Ce_{0.9}Sm_{0.1}O_{2-\delta}$ nanowires obtained by a hydrothermal method followed by the wet impregnation of Ni. (H) X-ray diffraction patterns and (I) Raman spectra for the obtained CeO_2, $Ce_{0.9}Sm_{0.1}O_{2-\delta}$, and $Ni/Ce_{0.9}Sm_{0.1}O_{2-\delta}$ nanowires.

and are essential for high-performance catalysts.

In order to better understand the effect of the nanowires, Ni-based catalysts were prepared using different supports. The addition of Ni (1 wt%) was carried out over both CeO_2 and Sm_2O_3 nanowires, and commercial CeO_2 and Sm_2O_3 samples for comparison. Chemical analysis by EDX spectra (Fig. S4) showed that all samples have compositions very similar to the nominal ones.

Fig. S5 depicts the CO-TPD profiles for all prepared nickel-based catalysts. In all cases, when nickel was supported onto the surface of nanowires (black traces), the CO-TPD profiles presented better-defined peaks with less intense shoulders. Such a feature indicates similar levels of reactivity of the Ni species, in agreement with the formation of well-defined catalysts displaying a controlled structure (support and active phase) [44–46]. On the other hand, for the catalysts based on commercial supports (red traces), multiple peaks at different temperatures were observed indicating different reactivities among the Ni sites, which indicates more heterogeneous nanomaterials [44–46].

The specific and metallic surface area were measured by BET and CO chemisorption analyses, respectively, and listed in Table 1. Herein, specific surface area values obtained for the nanowires were much higher than those of catalysts prepared from commercial materials, in agreement with the formation of uniform nano-structured materials [47]. Interestingly, metallic (Ni) surface area were higher for the nanowires than that for the catalysts prepared from commercial materials, a feature possibly related to the well-defined morphology of the nanowire supports [48]. The formation of $Ni/Ce_{0.9}Sm_{0.1}O_{2-\delta}$ nanowire catalyst was supported by X-ray diffraction (Fig. 1H) and Raman spectroscopy (Fig. 1I). The complete XRD data set for all produced catalysts is shown in the Fig. S6. Both nanowires and particles of commercial ceria samples exhibited similar XRD patterns indicating that the nanowire synthesis resulted in single-phase crystalline materials. However, it can be observed that the XRD patterns for nanowires exhibited broader peaks as compared with their counterparts with the same composition, indicating the smaller crystallite size of nanowires [24]. The XRD patterns of the $Ce_{0.9}Sm_{0.1}O_{2-\delta}$ nanowires are similar to that of CeO_2 nanowires (Fig. 1H). However, slight shifts were observed in all diffraction angles of the Sm-doped samples indicating that the dopant was incorporated in the fluorite lattice, similarly to previously reported results of doped-ceria materials [49]. No diffraction peaks related to Sm-based species were observed, confirming the the

Table 1
Surface properties of the obtained catalysts measured by N_2 physisorption and CO chemisorption.

Sample	Surface area ($m^2\ g^{-1}$ catalyst)			Metallic area (μmol g^{-1} metal)		
	Nanowires	Commercial	Increase (folds)	Nanowires	Commercial	Increase (folds)
CeO_2	87.2	9.2	9.5	–	–	–
Sm_2O_3	54.5	7.9	6.9	–	–	–
$Ce_{0.9}Sm_{0.1}O_{2-\delta}$	98.4	11.9	8.3	–	–	–
Ni/CeO_2	85.0	8.7	9.8	16.28	6.80	2.4
Ni/Sm_2O_3	52.5	7.8	6.7	16.33	6.98	2.3
$Ni/Ce_{0.9}Sm_{0.1}O_{2-\delta}$	88.7	9.6	9.2	18.20	6.01	3.0

formation of a solid solution [49]. The XRD data showed no diffraction peaks related to Ni-based species, probably because both the low loading and fine distribution of the metal in the $Ce_{0.9}Sm_{0.1}O_{2-\delta}$ (1 wt%) nanowires.

Raman spectra for the CeO_2, $Ce_{0.9}Sm_{0.1}O_{2-\delta}$, and $Ni/Ce_{0.9}Sm_{0.1}O_{2-\delta}$ nanowires confirmed the main features of XRD analysis (Fig. 1I) [24,50]. The Raman profile of both the CeO_2 and the Sm-doped ceria structures were similar, and no peaks associated with Sm-based species were observed. $Ce_{0.9}Sm_{0.1}O_{2-\delta}$ nanowires displayed an intense peak centered at 453 cm^{-1} associated with oxygen atoms around Ce^{4+} ions whereas $Ni/Ce_{0.9}Sm_{0.1}O_{2-\delta}$ nanowires presented additional peaks at 520, 641, and 780 cm^{-1} related to one-phonon, two-phonon, and two-phonon scattering of the NiO structure, respectively [51]. Raman data revealed additional features such as broad and intense peaks around 455 cm^{-1} and a low intensity peak centered at 601 cm^{-1}. Such peaks were previously related to the formation of ceria nanomaterials having relatively high concentration of oxygen vacancies in the fluorite structure [24,50]. Such finding is very interesting for catalytic applications, specially for ethanol steam reforming in which the enrichment of oxygen vacancies onto the catalysts surface prevents carbon species deposition and, consequently, enhances catalyst stability. The generation of oxygen vacancies ($V_{O^{\cdot\cdot}}$) with the addition of Sm^{3+} species in the structure of CeO_2 can be represented as indicated by Eq. (12), in which a Sm-deped ceria structure (Sm'_{Ce}) is obtained together with molecular oxygen (O2) [52]:

$$2\,Sm^{3+} \overset{CeO_2}{\rightarrow} 2\,Sm'_{ce} + V_{O^{\cdot\cdot}} + \frac{1}{2}O_2 \quad (12)$$

The TPR profiles for the CeO_2, $Ce_{0.9}Sm_{0.1}O_{2-\delta}$, and $Ni/Ce_{0.9}Sm_{0.1}O_{2-\delta}$ nanowires (Fig. S7) are in agreement with the Raman data. The CeO_2 nanowires presented two broad and intense peaks centered at 655 and 958 °C that are assigned to the reduction of bulk and surface ceria [24,53]. The addition of Sm in the structure of CeO_2 and Ni onto the surface of the $Ce_{0.9}Sm_{0.1}O_{2-\delta}$ nanowires shifted the reduction peaks to lower temperatures indicating an increase in their reducibility properties and the enrichment of oxygen vacancies [18,54]. In the TPR profile for the $Ni/Ce_{0.9}Sm_{0.1}O_{2-\delta}$ nanowires, the peak centered at 365 °C is associated with the reduction of NiO to Ni [55]. The complete TPR data for all produced catalysts are depicted in the Fig. S8. For all samples, it can be observed that all the reduction peaks were shifted to lower temperatures compared with their catalysts prepared from commercial materials counterparts with the same composition, which also indicate an increase in their reducibility properties and the enrichment of oxygen vacancies [18,54].

In order to indentify surface composition and gain further insights about the synthesized catalysts, X-ray photoelectron spectroscopy (XPS) analyzes (Fig. 2 and Table 2) were performed. Fig. 2A shows the O 1s XPS spectra of the CeO_2, $Ce_{0.9}Sm_{0.1}O_{2-\delta}$, and $Ni/Ce_{0.9}Sm_{0.1}O_{2-\delta}$ nanowires. The XPS spectra showed three different surface oxygen species: i) lattice oxygen (O_L) with binding energy between 529.9 and 529.5 eV, ii) surface oxygen ions or oxygen vacancies (O_S) with binding energy 532.0–531.4 eV, and adsorbed water (O_w) with binding energies around 533.9 eV [56]. Interestingly, in agreement with both the Raman spectroscopy and TPR analyses, the O 1s XPS spectra showed that Sm doping in the CeO_2 structure (leading to the formation of $Ce_{0.9}Sm_{0.1}O_{2-\delta}$ nanowires) followed by the addition of Ni (obtaining $Ni/Ce_{0.9}Sm_{0.1}O_{2-\delta}$ nanowires) generated a significant increase in percentage of oxygen vacancies or surface oxygen ions at the nanowires surface. The values of the percentage of oxygen vacancies or surface oxygen ions corresponded to 57, 63, and 67% for the CeO_2, $Ce_{0.9}Sm_{0.1}O_{2-\delta}$, and $Ni/Ce_{0.9}Sm_{0.1}O_{2-\delta}$ nanowires, respectively. In addition, the Ce 3d XPS spectra for the nanowires (Fig. 2B) indicated the presence of both Ce^{3+} and Ce^{4+} species, which can be associated with different profiles: Ce^{3+} (v_0, v′, u_0 and u′) and Ce^{4+} (v, v″, v‴, u, u″, and u‴) [57,58]. Thus, according with previous studies, u′ and u‴ are directly associated with the concentration of Ce^{3+} and Ce^{4+} ions, respectively [57,58]. For all analyzed nanowires, the percentages of Ce^{3+} and Ce^{4+} ions kept similar, indicating that the enrichment of oxygen vacancies or oxygen ions at the nanowires surface can be associated with the addition of Sm^{3+} ions (Fig. 2C) in order to maintain the electrostatic balance of the CeO_2 lattice and also the formation of NiO in the case of $Ni/Ce_{0.9}Sm_{0.1}O_{2-\delta}$ nanowires (Fig. 2D) [59,60]. Herein, XPS spectra of the $Ni/Ce_{0.9}Sm_{0.1}O_{2-\delta}$ nanowires showed two peaks centered at binding energies of 854.3and 859.9 eV, which correspond to NiO and its satellite, respectively [61].

Here, we can highlight the combination of exceptional properties that make possible the application of the $Ni/Ce_{0.9}Sm_{0.1}O_{2-\delta}$ nanowires as an effective catalyst towards ethanol steam reforming and, possibly, many other reactions: i) higher surface area (specially as compared to samples with the same composition), ii) small thicknesses, iii) high concentration of oxygen vacancies at the surface, and iv) fine distribution of Ni at the surface of the nanowires with superior metallic surface area [24,56,62,63], Thus, following synthesis and characterization of nanowire catalysts, we turned our attention to the investigation of the catalytic performance towards the ethanol steam reforming.

Initially, to optimize the catalytic performance of the $Ni/Ce_{0.9}Sm_{0.1}O_{2-\delta}$ nanowires, especially concerning the H_2 production and ethanol conversion, a series of experiments studing the ethanol conversion and products distribution as a function of temperature (Fig. S9A) and H_2O/CH_3CH_2OH molar ratio (Fig. S9B) were performed to compare the equilibrium values (24 h of reaction) obtained for each condition. The complete profiles for temperature and H_2O/CH_3CH_2OH molar ratio studies are available in the Figs. S10 and S11, respectively. Using the H_2O/CH_3CH_2OH molar ratio = 3, which is the theoretical stechiometric ratio, the ethanol is completely converted at 400 °C and the H_2 production has a maximum peak at 550 °C. This result is in agreement with previous studies that evidenced temperatures in the range of 450–600 °C showed the best values for performances in terms of both ethanol conversion and H_2 selectivity [55,64,65]. Thus, 550 °C was fixed to further investigate the catalytic properties of the nanowire catalysts. Reactions varying the H_2O/CH_3CH_2OH molar revealed that ratios 3 and 1 were the best values for the reforming reaction. In such conditions, selectivities of H_2 around 60% of were observed. However, using the H_2O/CH_3CH_2OH molar ratio 1, a higher CO production was detected. Thus, the H_2O/CH_3CH_2OH molar ratio of 3 was choosen as the best option due to the need of greener processes, in which the lowest CO production is desired [66].

Fig. 3 shows the time dependence of both ethanol conversion (%) and product selectivity for ethanol steam reforming using the nanowires catalysts. Interestingly, when pure CeO_2 (Fig. 3A) and $Ce_{0.9}Sm_{0.1}O_{2-\delta}$ (Fig. 3B) nanowires were employed as catalysts, the complete ethanol conversion was observed at 550 °C over the entire period of 24 h of reaction. However, low values for H_2 production were observed (~15%) due to the need of metals such as nickel, cobalt, or rhodium to promote the ethanol steam reforming (Eq. (13)). [66]

$$CH_3CH_2OH_{(g)} + 3H_2O_{(g)} \rightarrow 2CO_{2(g)} + 6H_{2(g)} \quad (13)$$

Here, the major product for both catalysts was ethene (C_2H_4), which is usually produced by the ethanol dehydration (Eq. (14)) under our reported conditions [36].

$$CH_3CH_2OH_{(g)} \rightarrow C_2H_{4(g)} + H_2O_{(g)} \quad (14)$$

Carbon monoxide, methane, acetone, and acetaldehyde were also observed as products, which can be formed according the Eqs. (15)–(17) [36].

$$CH_3CH_2OH_{(g)} \rightarrow CO_{(g)} + CH_{4(g)} + H_{2(g)} \quad (15)$$

$$CH_3CH_2OH_{(g)} \rightarrow CH_3CHO_{(g)} + H_{2(g)} \quad (16)$$

$$2CH_3CH_2OH_{(g)} \rightarrow CH_3(CO)CH_{3(g)} + CO_{(g)} + 3H_{2(g)} \quad (17)$$

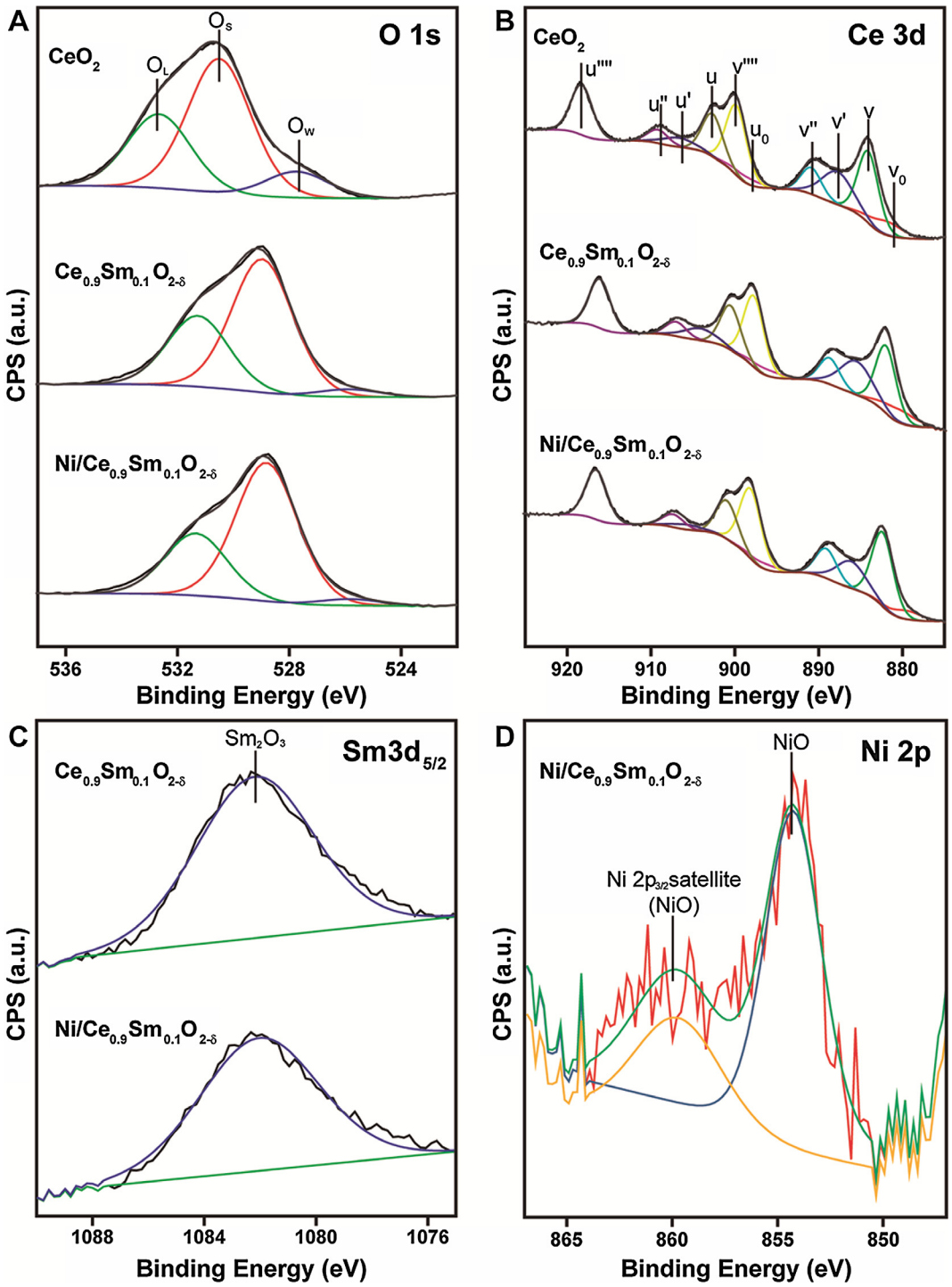

Fig. 2. XPS spectra of the (A) O 1s, (B) Ce 3d, (C) Sm $3d_{5/2}$, and (D) Ni 2p for the obtained CeO_2, $Ce_{0.9}Sm_{0.1}O_{2-\delta}$, and $Ni/Ce_{0.9}Sm_{0.1}O_{2-\delta}$ nanowires.

As expected, Ni incorporation onto the $Ce_{0.9}Sm_{0.1}O_{2-\delta}$ nanowires surfaces promoted the steam reforming reaction of ethanol (Fig. 3C). By adding Ni, mostly ethanol steam reforming products were obtained and a significant increase in the selectivity for H_2 production, achieving ~60%, was observed. Moreover, the long-time stability observed of such catalyst is remarkable. Long term testing of $Ni/Ce_{0.9}Sm_{0.1}O_{2-\delta}$ nanowires showed no deactivation after 192 h (8 days) of reaction at 550 °C under practical conditions of a typical steam reforming system. Such result agrees with the characterization results that revealed fine Ni particles and high concentration of surface oxygen species, which tend to prevent deactivation processes. For comparison, Ni/CeO_2 nanowires (Fig. S12) were also employed as catalyst towards the ethanol steam reforming. Herein, mostly products derived from ethanol steam reforming reaction were observed (CO_2 and H_2) with the production of methane (~0.5%) and carbon monoxide (~10%) as by-products. However, the selectivity for the hydrogen production was severely limited (~35%), especially comparing to the recent results showing values ~60% [13,17,19,36,67]. Such results evidenced the relevant role of the rare-earth dopped support on the ethanol reforming providing sufficient oxygen species that contribute to both hydrogen selectivity and stability.

Furthermore, as depicted in Fig. 4A, the overall morphology of Ni/

Table 2
XPS binding energies, u′/u‴, and Os/O_L ratio obtained from the Ce 3d and O 1s regions for the synthesized nanowires.

Sample	Binding energy Ce 3d (eV)		Binding energy O 1s (eV)		
	u′	u‴	O_L	O_S	O_S/O_L
CeO_2	906.7 (3.8)*	918.3 (14.1)*	527.7 (11)*	530.5 (57)*	5
$Ce_{0.9}Sm_{0.1}O_{2-\delta}$	904.1 (5.0)*	916.0 (13.6)*	525.7 (4)*	528.9 (63)*	15
$Ni/Ce_{0.9}Sm_{0.1}O_{2-\delta}$	905.7 (2.1)*	916.5 (14.81)*	525.7 (3)*	528.7 (67)*	22

* Percentages of $Ce^{\delta+}$, Sm, Ni, or O species.

$Ce_{0.9}Sm_{0.1}O_{2-\delta}$ nanowires remained unchanged after 192 h of reaction at 550 °C. Moreover, careful analysis of spent catalyst revealed no detectable carbon deposits or filaments, as usually observed in deactivated catalysts [68–70]. In addition, XRD (Fig. 4B), CO-TPD (Fig. 4C), and TGA (Fig. 4D) analyses after steam reforming reaction confirmed the robustness of the nanowire catalyst, in which no significant changes were observed on both XRD and CO-TPD profiles. In the TGA analysis, a total weight loss of 5.6% was observed after heating up to 1000 °C. However, a significant mass loss event (2.7%) takes place at low temperatures (~150 °C) is attributed to the release of adsorbed waterfrom the catalyst surface. Therefore, the mass loss that can be related to the oxidation of carbon-based materials after the ethanol steam reforming occurs at temperatures above 150 °C and corresponds to 2.9%. Such amount of carbon represents a minor fraction (0.07%) of all carbon fed over the 192 h of reaction and the calculated fraction o carbon mass is 0.15 mgC $g_{cat}^{-1}h^{-1}$. For comparison, in systems operated under similar conditions to this study, the typical fraction of carbon deposition as a function of amount of catalyst and time is reported in the range of 6–30 mgC $g_{cat}^{-1}h^{-1}$, which is more than 40–200 times higher than that obtained in this study [71–73]. BET and CO chemisorption analyses were also performed after the stability experiment. Here, the values of specific and metallic surface area of the $Ni/Ce_{0.9}Sm_{0.1}O_{2-\delta}$ nanowires remained almost unchanged and corresponded to 85.9 $m^2 g^{-1}$ and 17.35 μmol g^{-1} metal, respectively. Such values are comparable to those obtained for the fresh catalyst: 88.7 m^2 g^{-1} and 18.20 μmol g^{-1} metal for the specific and metallic surface area, respectively (Table 1). Such features are consistent with the high stability of the catalyst and indicate the maintenance of the structures of both the $Ce_{0.9}Sm_{0.1}O_{2-\delta}$ nanowires support and the surface layer of nickel after steam reforming of ethanol under our experimental conditions.

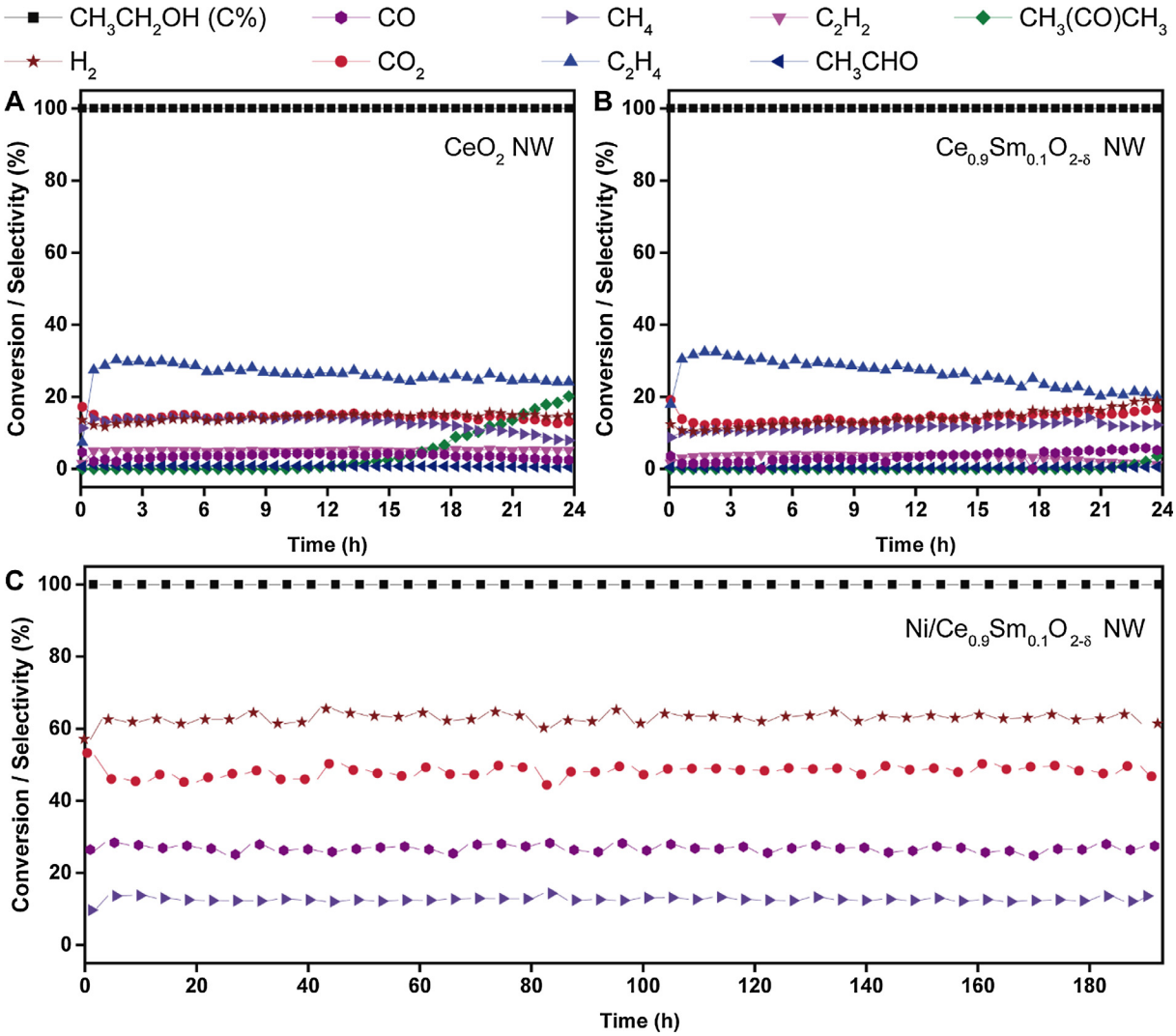

Fig. 3. Ethanol conversion and product selectivities obtained in the presence of (A) CeO_2, (B) $Ce_{0.9}Sm_{0.1}O_{2-\delta}$, and (C) $Ni/Ce_{0.9}Sm_{0.1}O_{2-\delta}$ nanowires as catalysts. The experiments were performed at 550 °C and H_2O/CH_3CH_2OH molar ratio = 3. The stability experiment performed using $Ni/Ce_{0.9}Sm_{0.1}O_{2-\delta}$ nanowires as catalysts is shown in (C).

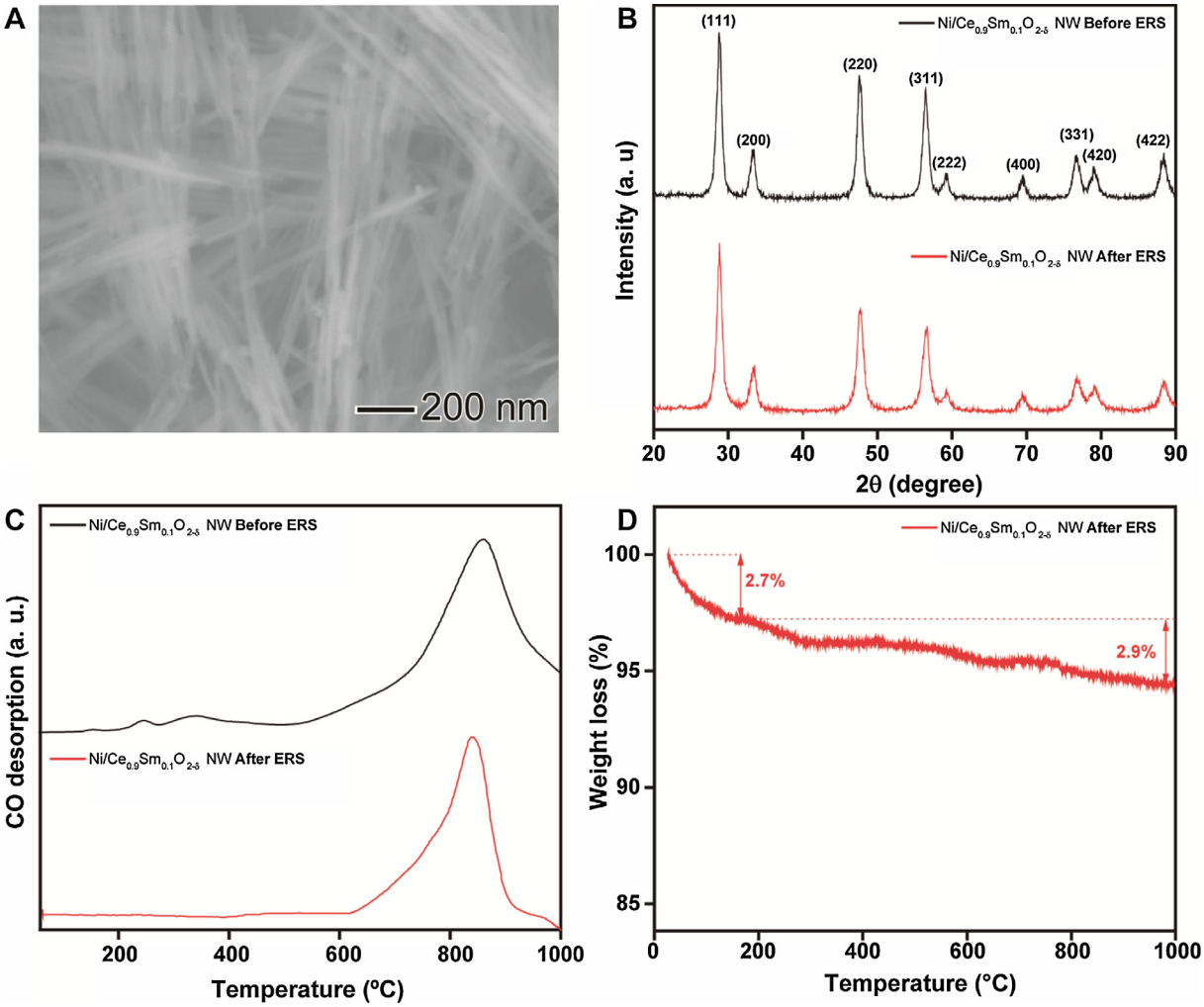

Fig. 4. (A) SEM image (before the stability experiment), (B) XRD profiles, (C) CO-TPD profiles, and (D) TGA profile for Ni/$Ce_{0.9}Sm_{0.1}O_{2-\delta}$ nanowires before and after the stability experiment.

4. Conclusions

In summary, we have demonstrated the synthesis of Ni/$Ce_{0.9}Sm_{0.1}O_{2-\delta}$ nanowires displaying well-defined shape, size, and composition, which presented superior performance towards the ethanol steam reforming as compared to catalysts prepared from commercial materials. In contrast to conventional procedures, which are usually limited in terms of productivity and control over the nanoparticle properties, our reported Ni/$Ce_{0.9}Sm_{0.1}O_{2-\delta}$ nanowires could be obtained by a facile and high yield two step synthesis: i) a hydrothermal synthesis ($Ce_{0.9}Sm_{0.1}O_{2-\delta}$ nanowires) followed by ii) the wet impregnation of Ni. Herein, the resulting catalyst showed superior properties that included higher surface area, well-defined structural properties, high concentration of oxygen vacancies at their surface, and a fine distribution of Ni at the surface with superior metallic surface area. Such features indicate the nanowire catalyst as very attractive material for large-scale production and utilization for ethanol steam reforming reaction. The special performance, with high production of hydrogen (~60% of selectivity) and long-term stability at 550 °C under practical conditions of a typical steam reforming system. Thus, our results demonstrate that the synthesis of catalysts with controlled properties can represent a promising strategy for enabling practical applications in heterogeneous catalysis, in which simple, fast, and scalable procedures are strongly desired.

Acknowledgments

This work was supported by FAPESP (grant number 2014/09087-4, 2014/50279-4, and scholarship 2017/04929-5). F.C.F, M. L., and P.H.C.C. thank the CNPq for their research fellowships. T.S.R., A.G.M.S., and J. J. Q thank FAPESP for their fellowships. E.G.C. and F.A.S. thank CNPq for their fellowships. We thank the Brazilian Synchrotron Light Laboratory (LNLS) for the access to the XPS facility.

Appendix A. Supplementary data

Supplementary data to this article can be found online at https://doi.org/10.1016/j.fuel.2018.10.053.

References

[1] Goldemberg J. Ethanol for a sustainable energy future. Science (80-) 2007;315(808). LP-810.
[2] Steil MC, Nobrega SD, Georges S, Gelin P, Uhlenbruck S, Fonseca FC. Durable direct ethanol anode-supported solid oxide fuel cell. Appl Energy 2017;199:180–6. https://doi.org/10.1016/j.apenergy.2017.04.086.
[3] Klouz V, Fierro V, Denton P, Katz H, Lisse JP, Bouvot-Mauduit S, et al. Ethanol reforming for hydrogen production in a hybrid electric vehicle: process optimisation. J Power Sources 2002;105:26–34. https://doi.org/10.1016/S0378-7753(01)00922-3.
[4] Mattos LV, Jacobs G, Davis BH, Noronha FB. Production of hydrogen from ethanol: review of reaction mechanism and catalyst deactivation. Chem Rev 2012;112:4094–123. https://doi.org/10.1021/cr2000114.

[5] Palo DR, Dagle RA, Holladay JD. Methanol Steam Reforming for Hydrogen Production. Chem Rev 2007;107:3992–4021. https://doi.org/10.1021/cr050198b.

[6] Chen HL, Lee HM, Chen SH, Chao Y, Chang MB. Review of plasma catalysis on hydrocarbon reforming for hydrogen production—Interaction, integration, and prospects. Appl Catal B Environ 2008;85:1–9. https://doi.org/10.1016/j.apcatb.2008.06.021.

[7] Vaidya PD, Rodrigues AE. Glycerol reforming for hydrogen production: a review. Chem Eng Technol 2009;32:1463–9. https://doi.org/10.1002/ceat.200900120.

[8] Greluk M, Słowik G, Rotko M, Machocki A. Steam reforming and oxidative steam reforming of ethanol over PtKCo/CeO2 catalyst. Fuel 2016;183:518–30. https://doi.org/10.1016/j.fuel.2016.06.068.

[9] Li T, Zhang J, Xie X, Yin X, An X. Montmorillonite-supported Ni nanoparticles for efficient hydrogen production from ethanol steam reforming. Fuel 2015;143:55–62. https://doi.org/10.1016/j.fuel.2014.11.033.

[10] Chen M, Wang Y, Yang Z, Liang T, Liu S, Zhou Z, et al. Effect of Mg-modified mesoporous Ni/Attapulgite catalysts on catalytic performance and resistance to carbon deposition for ethanol steam reforming. Fuel 2018;220:32–46. https://doi.org/10.1016/j.fuel.2018.02.013.

[11] Chaubey R, Sahu S, James OO, Maity S. A review on development of industrial processes and emerging techniques for production of hydrogen from renewable and sustainable sources. Renew Sustain Energy Rev 2013;23:443–62. https://doi.org/10.1016/j.rser.2013.02.019.

[12] Zanchet D, Santos JBO, Damyanova S, Gallo JMR, Bueno JMC. Toward understanding metal-catalyzed ethanol reforming. ACS Catal 2015;5:3841–63. https://doi.org/10.1021/cs5020755.

[13] Ni M, Leung DYC, Leung MKH. A review on reforming bio-ethanol for hydrogen production. Int J Hydrogen Energy 2007;32:3238–47. https://doi.org/10.1016/j.ijhydene.2007.04.038.

[14] Panagiotopoulou P, Verykios XE. Mechanistic aspects of the low temperature steam reforming of ethanol over supported Pt catalysts. Int J Hydrogen Energy 2012;37:16333–45. https://doi.org/10.1016/j.ijhydene.2012.02.087.

[15] Karim AM, Su Y, Sun J, Yang C, Strohm JJ, King DL, et al. A comparative study between Co and Rh for steam reforming of ethanol. Appl Catal B Environ 2010;96:441–8. https://doi.org/10.1016/j.apcatb.2010.02.041.

[16] Haryanto A, Fernando S, Murali N, Adhikari S. Current status of hydrogen production techniques by steam reforming of ethanol: a review. Energy Fuels 2005;19:2098–106. https://doi.org/10.1021/ef0500538.

[17] Riani P, Garbarino G, Lucchini MA, Canepa F, Busca G. Unsupported versus alumina-supported Ni nanoparticles as catalysts for steam/ethanol conversion and CO2 methanation. J Mol CatalA Chem 2014;383–384:10–6. https://doi.org/10.1016/j.molcata.2013.11.006.

[18] Soykal II, Sohn H, Ozkan US. Effect of support particle size in steam reforming of ethanol over Co/CeO2 catalysts. ACS Catal 2012;2:2335–48. https://doi.org/10.1021/cs3004159.

[19] Fajardo H, Longo E, Mezalira D, Nuernberg G, Almerindo G, Collasiol A, et al. Influence of support on catalytic behavior of nickel catalysts in the steam reforming of ethanol for hydrogen production. Environ Chem Lett 2010;8:79–85. https://doi.org/10.1007/s10311-008-0195-5.

[20] Dan M, Mihet M, Tasnadi-Asztalos Z, Imre-Lucaci A, Katona G, Lazar MD. Hydrogen production by ethanol steam reforming on nickel catalysts: effect of support modification by CeO2 and La2O3. Fuel 2015;147:260–8. https://doi.org/10.1016/j.fuel.2015.01.050.

[21] Gupta A, Waghmare UV, Hegde MS. Correlation of oxygen storage capacity and structural distortion in transition-metal-, noble-metal-, and rare-earth-ion-substituted CeO2 from first principles calculation. Chem Mater 2010;22:5184–98. https://doi.org/10.1021/cm101145d.

[22] Kehoe AB, Scanlon DO, Watson GW. Role of lattice distortions in the oxygen storage capacity of divalently doped CeO2. Chem Mater 2011;23:4464–8. https://doi.org/10.1021/cm201617d.

[23] Rodrigues TS, da Silva AHM, da Silva AGM, Ceara DG, Gomes JF, Assaf JM, et al. Hollow AgPt/SiO2 nanomaterials with controlled surface morphologies: is the number of Pt surface atoms imperative to optimize catalytic performances? Catal Sci Technol 2016;6:2162–70. https://doi.org/10.1039/C5CY01415H.

[24] Silva AGM, Rodrigues TS, Dias A, Fajardo HV, Goncalves RF, Godinho M, et al. Ce1-xSmxO1.9-[small delta] nanoparticles obtained by microwave-assisted hydrothermal processing: an efficient application for catalytic oxidation of [small alpha]-bisabolol. Catal Sci Technol 2014;4:814–21. https://doi.org/10.1039/C3CY00788J.

[25] Krishna K, Bueno-López A, Makkee M, Moulijn JA. Potential rare earth modified CeO2 catalysts for soot oxidation: I. Characterisation and catalytic activity with O2. Appl Catal B Environ 2007;75:189–200. https://doi.org/10.1016/j.apcatb.2007.04.010.

[26] Matsumoto S. Recent advances in automobile exhaust catalysts. Catal Today 2004;90:183–90. https://doi.org/10.1016/j.cattod.2004.04.048.

[27] Guo M, Lu J, Wu Y, Wang Y, Luo M. UV and visible raman studies of oxygen vacancies in rare-earth-doped ceria. Langmuir 2011;27:3872–7. https://doi.org/10.1021/la200292f.

[28] Moretti E, Storaro L, Talon A, Chitsazan S, Garbarino G, Busca G, et al. Ceria–zirconia based catalysts for ethanol steam reforming. Fuel 2015;153:166–75. https://doi.org/10.1016/j.fuel.2015.02.077.

[29] Li C, Sun Y, Djerdj I, Voepel P, Sack C-C, Weller T, et al. Shape-controlled CeO2 nanoparticles: stability and activity in the catalyzed HCl oxidation reaction. ACS Catal 2017;7:6453–63. https://doi.org/10.1021/acscatal.7b01618.

[30] Qiao Z-A, Wu Z, Dai S. Shape-controlled ceria-based nanostructures for catalysis applications. ChemSusChem 2013;6:1821–33. https://doi.org/10.1002/cssc.201300428.

[31] Controlled Ru-Shi L. Nanofabrication: advances and applications. Pan Stanford Publishing; 2012.

[32] Tao Y, Wang H, Xia Y, Zhang G, Wu H, Tao G. Preparation of shape-controlled CeO2 nanocrystals via microwave-assisted method. Mater Chem Phys 2010;124:541–6. https://doi.org/10.1016/j.matchemphys.2010.07.007.

[33] Pan C, Zhang D, Shi L, Fang J. Template-free synthesis, controlled conversion, and CO oxidation properties of CeO2 nanorods, nanotubes, nanowires, and nanocubes. Eur J Inorg Chem 2008;2008:2429–36. https://doi.org/10.1002/ejic.200800047.

[34] Shi W, Song S, Zhang H. Hydrothermal synthetic strategies of inorganic semiconducting nanostructures. Chem Soc Rev 2013;42:5714–43. https://doi.org/10.1039/C3CS60012B.

[35] Rodrigues TS, da Silva AGM, Gonçalves MC, Fajardo HV, Balzer R, Probst LFD, et al. AgPt hollow nanodendrites: synthesis and uniform dispersion over SiO2 support for catalytic applications. ChemNanoMat 2015;1:46–51. https://doi.org/10.1002/cnma.201500025.

[36] Palma V, Castaldo F, Ciambelli P, Iaquaniello G. CeO2-supported Pt/Ni catalyst for the renewable and clean H2 production via ethanol steam reforming. Appl Catal B Environ 2014;145:73–84. https://doi.org/10.1016/j.apcatb.2013.01.053.

[37] da Silva A, Batalha D, Rodrigues T, Candido E, Luz S, De Freitas I, et al. Towards the Sub-15nm CeO2 nanowires with increased oxygen defects and Ce3+ sites for selective oxidation of aniline at room-temperature with a non-noble metal catalyst. Catal Sci Technol 2018. https://doi.org/10.1039/C7CY02402A.

[38] Ketzial JJ, Nesaraj AS. Wet chemical synthesis and physical characterization of doped CeO2 nanoparticles. J Nanoanalysis 2014;1:110–24. https://doi.org/10.22034/jna.2014.03.002.

[39] Zhou K, Wang X, Sun X, Peng Q, Li Y. Enhanced catalytic activity of ceria nanorods from well-defined reactive crystal planes. J Catal 2005;229:206–12. https://doi.org/10.1016/j.jcat.2004.11.004.

[40] Pérez-Hernández R, Mondragón-Galicia G, Allende Maravilla A, Palacios J. Nanodimensional CeO2 nanorods for high Ni loading catalysts: H2 production by autothermal steam reforming of methanol reaction. PCCP 2013;15:12702–8. https://doi.org/10.1039/C3CP52032C.

[41] Silva AGM, Rodrigues TS, Taguchi LSK, Fajardo HV, Balzer R, Probst LFD, et al. Pd-based nanoflowers catalysts: controlling size, composition, and structures for the 4-nitrophenol reduction and BTX oxidation reactions. J Mater Sci 2015;51:603–14. https://doi.org/10.1007/s10853-015-9315-3.

[42] Rodrigues TS, da Silva AGM, Gonçalves MC, Fajardo HV, Balzer R, Probst LFD, et al. Catalytic properties of AgPt nanoshells as a function of size: larger outer diameters lead to improved performances. Langmuir 2016;32:9371–9. https://doi.org/10.1021/acs.langmuir.6b01783.

[43] Jiang SP. A review of wet impregnation—An alternative method for the fabrication of high performance and nano-structured electrodes of solid oxide fuel cells. Mater Sci Eng, A 2006;418:199–210. https://doi.org/10.1016/j.msea.2005.11.052.

[44] Velu S, Gangwal SK. Synthesis of alumina supported nickel nanoparticle catalysts and evaluation of nickel metal dispersions by temperature programmed desorption. Solid State Ionics 2006;177:803–11. https://doi.org/10.1016/j.ssi.2006.01.031.

[45] Niwa M, Katada N. New method for the temperature- programmed desorption (TPD) of ammonia experiment for characterization of zeolite acidity: a review. Chem Rec 2013;13:432–55. https://doi.org/10.1002/tcr.201300009.

[46] Bhatia S, Beltramini J, Do DD. Temperature programmed analysis and its applications in catalytic systems. Catal Today 1990;7:309–438. https://doi.org/10.1016/0920-5861(90)87001-J.

[47] da Silva AGM, Batalha DC, Rodrigues TS, Candido EG, Luz SC, de Freitas IC, et al. Sub-15 nm CeO2 nanowires as an efficient non-noble metal catalyst in the room-temperature oxidation of aniline. Catal Sci Technol 2018;8:1828–39. https://doi.org/10.1039/C7CY02402A.

[48] Jiménez-Gómez CP, Cecilia JA, Moreno-Tost R, Maireles-Torres P. Nickel phosphide/silica catalysts for the gas-phase hydrogenation of furfural to high-–added–value chemicals. ChemCatChem 2017;9:2881–9. https://doi.org/10.1002/cctc.201700312.

[49] Rangaswamy A, Sudarsanam P, Reddy BM. Rare earth metal doped CeO2-based catalytic materials for diesel soot oxidation at lower temperatures. J Rare Earths 2015;33:1162–9. https://doi.org/10.1016/S1002-0721(14)60541-X.

[50] Wu Z, Li M, Howe J, Meyer HM, Overbury SH. Probing defect sites on CeO2 nanocrystals with well-defined surface planes by Raman spectroscopy and O2 adsorption. Langmuir 2010;26:16595–606. https://doi.org/10.1021/la101723w.

[51] Pärs NM-U, Kuzmin A, Steins I, Grabis J, Sildos I, Pärs M. Raman scattering in nanosized nickel oxide NiO. J Phys Conf Ser 2007;93:12039.

[52] Babu S, Thanneeru R, Inerbaev T, Day R, Masunov AE, Schulte A, et al. Dopant-mediated oxygen vacancy tuning in ceria nanoparticles. Nanotechnology 2009;20:85713.

[53] Pal P, Pahari SK, Sinhamahapatra A, Jayachandran M, Kiruthika GVM, Bajaj HC, et al. CeO2 nanowires with high aspect ratio and excellent catalytic activity for selective oxidation of styrene by molecular oxygen. RSC Adv 2013;3:10837–47. https://doi.org/10.1039/C3RA23485A.

[54] Alhumaimess M, Lin Z, He Q, Lu L, Dimitratos N, Dummer NF, et al. Oxidation of benzyl alcohol and carbon monoxide using gold nanoparticles supported on MnO2 nanowire microspheres. Chem – A Eur J 2014;20:1701–10. https://doi.org/10.1002/chem.201303355.

[55] da Silva AAA, Bion N, Epron F, Baraka S, Fonseca FC, Rabelo-Neto RC, et al. Effect of the type of ceria dopant on the performance of Ni/CeO2 SOFC anode for ethanol internal reforming. Appl Catal B Environ 2017;206:626–41. https://doi.org/10.1016/j.apcatb.2017.01.069.

[56] da Silva AGM, Kisukuri CM, Rodrigues TS, Candido EG, de Freitas IC, da Silva AHM, et al. MnO2 nanowires decorated with Au ultrasmall nanoparticles for the green oxidation of silanes and hydrogen production under ultralow loadings. Appl Catal B

Environ 2016;184:35–43. https://doi.org/10.1016/j.apcatb.2015.11.023.
[57] Younis A, Chu D, Li S. Oxygen level: the dominant of resistive switching characteristics in cerium oxide thin films. J Phys D Appl Phys 2012;45:355101.
[58] Baron M, Bondarchuk O, Stacchiola D, Shaikhutdinov S, Freund H-J. Interaction of Gold with Cerium Oxide Supports: CeO2(111) Thin Films vs CeOx Nanoparticles. J Phys Chem C 2009;113:6042–9. https://doi.org/10.1021/jp9001753.
[59] Venkataswamy P, Rao KN, Jampaiah D, Reddy BM. Nanostructured manganese doped ceria solid solutions for CO oxidation at lower temperatures. Appl Catal B Environ 2015;162:122–32. https://doi.org/10.1016/j.apcatb.2014.06.038.
[60] Acharya SA, Gaikwad VM, D'Souza SW, Barman SR. Gd/Sm dopant-modified oxidation state and defect generation in nano-ceria. Solid State Ionics 2014;260:21–9. https://doi.org/10.1016/j.ssi.2014.03.008.
[61] Mansour AN. Characterization of NiO by XPS. Surf Sci Spectra 1994;3:231–8. https://doi.org/10.1116/1.1247751.
[62] Lee S, Nam G, Sun J, Lee J-S, Lee H-W, Chen W, et al. Enhanced intrinsic catalytic activity of λ-MnO2 by electrochemical tuning and oxygen vacancy generation. Angew Chemie Int Ed 2016;55:8599–604. https://doi.org/10.1002/anie.201602851.
[63] Mandal S, Bando KK, Santra C, Maity S, James OO, Mehta D, et al. Sm-CeO2 supported gold nanoparticle catalyst for benzyl alcohol oxidation using molecular O2. Appl Catal A Gen 2013;452:94–104. https://doi.org/10.1016/j.apcata.2012.11.030.
[64] Augusto BL, Noronha FB, Fonseca FC, Tabuti FN, Colman RC, Mattos LV. Nickel/gadolinium-doped ceria anode for direct ethanol solid oxide fuel cell. Int J Hydrogen Energy 2014;39:11196–209. https://doi.org/10.1016/j.ijhydene.2014.05.088.
[65] Nobrega SD, Gelin P, Georges S, Steil MC, Augusto BL, Noronha FB, et al. A fuel-flexible solid oxide fuel cell operating in gradual internal reforming. J Electrochem Soc 2014;161:F354–9. https://doi.org/10.1149/2.107403jes.
[66] Contreras JL, Salmones J, Colín-Luna JA, Nuño L, Quintana B, Córdova I, et al. Catalysts for H2 production using the ethanol steam reforming (a review). Int J Hydrogen Energy 2014;39:18835–53. https://doi.org/10.1016/j.ijhydene.2014.08.072.
[67] Li D, Zeng L, Li X, Wang X, Ma H, Assabumrungrat S, et al. Ceria-promoted Ni/SBA-15 catalysts for ethanol steam reforming with enhanced activity and resistance to deactivation. Appl Catal B Environ 2015;176–177:532–41. https://doi.org/10.1016/j.apcatb.2015.04.020.
[68] Postole G, Nguyen T-S, Aouine M, Gélin P, Cardenas L, Piccolo L. Efficient hydrogen production from methane over iridium-doped ceria catalysts synthesized by solution combustion. Appl Catal B Environ 2015;166–167:580–91. https://doi.org/10.1016/j.apcatb.2014.11.024.
[69] Florea M, Matei-Rutkovska F, Postole G, Urda A, Neatu F, Pârvulescu VI, et al. Doped ceria prepared by precipitation route for steam reforming of methane. Catal Today 2016. https://doi.org/10.1016/j.cattod.2016.12.006.
[70] Matei-Rutkovska F, Postole G, Rotaru CG, Florea M, Pârvulescu VI, Gelin P. Synthesis of ceria nanopowders by microwave-assisted hydrothermal method for dry reforming of methane. Int J Hydrogen Energy 2016;41:2512–25. https://doi.org/10.1016/j.ijhydene.2015.12.097.
[71] Wurzler GT, Rabelo-Neto RC, Mattos LV, Fraga MA, Noronha FB. Steam reforming of ethanol for hydrogen production over MgO—supported Ni-based catalysts. Appl Catal A Gen 2016;518:115–28. https://doi.org/10.1016/j.apcata.2015.11.020.
[72] Dantas SC, Resende KA, Ávila-Neto CN, Noronha FB, Bueno JMC, Hori CE. Nickel supported catalysts for hydrogen production by reforming of ethanol as addressed by in situ temperature and spatial resolved XANES analysis. Int J Hydrogen Energy 2016;41:3399–413. https://doi.org/10.1016/j.ijhydene.2015.12.164.
[73] Moraes TS, Neto RCR, Ribeiro MC, Mattos LV, Kourtelesis M, Verykios X, et al. Effects of ceria morphology on catalytic performance of Ni/CeO2 catalysts for low temperature steam reforming of ethanol. Top Catal 2015;58:281–94. https://doi.org/10.1007/s11244-015-0369-x.